

Synaptic density and neuronal metabolic function measured by PET in the unilateral 6-OHDA rat model of Parkinson's disease

1 Nakul Ravi Raval^{†1,2}, Frederik Gudmundsen^{†1}, Morten Juhl³, Ida Vang Andersen^{1,4}, Nikolaj
2 Raahauge Speth¹, Annesofie Videbæk¹, Ida Nyman Petersen⁵, Jens Damsgaard Mikkelsen^{1,6},
3 Patrick MacDonald Fisher¹, Matthias Manfred Herth^{4,5}, Pontus Plavén-Sigray¹, Gitte Moos
4 Knudsen^{1,2}, Mikael Palner^{*1,7,8}

5 ¹Neurobiology Research Unit, Copenhagen University Hospital (Rigshospitalet), DK-2100
6 Copenhagen, Denmark

7 ²Faculty of Health and Medical Sciences, University of Copenhagen, DK-2200 Copenhagen,
8 Denmark

9 ³Cardiology Stem Cell Centre, Copenhagen University Hospital (Rigshospitalet), DK-2100
10 Copenhagen, Denmark

11 ⁴Department of Drug Design and Pharmacology, Faculty of Health and Medical Sciences, University
12 of Copenhagen, DK-2100 Copenhagen, Denmark

13 ⁵Department of Clinical Physiology, Nuclear Medicine & PET, Copenhagen University Hospital
14 (Rigshospitalet), DK-2100 Copenhagen, Denmark.

15 ⁶Department of Neuroscience, University of Copenhagen, DK-2200 Copenhagen, Denmark

16 ⁷Department of Clinical Research, Clinical Physiology and Nuclear Medicine, University of Southern
17 Denmark, DK-5000 Odense, Denmark

18 ⁸Department of Nuclear Medicine, Odense University Hospital, DK-5000 Odense, Denmark

19 *** Correspondence:**

20 Mikael Palner

21 Neurobiology Research Unit

22 Section 8057, Rigshospitalet

23 Blegdamsvej 9

24 DK-2100 Copenhagen Ø

25 Denmark

26 Email: mikael.palner@nru.dk

27

28 [†]These authors have contributed equally to this work and share the first authorship.

29 **Keywords: Parkinson's disease, SV2A, FDG, PET, CSTC circuit, dopamine, 6-OHDA, UCB-J**

30 Abstract

31 Parkinson's disease (PD) is caused by progressive neurodegeneration and characterised by motor
32 dysfunction. Neurodegeneration of dopaminergic neurons also causes aberrations within the cortico-
33 striato-thalamo-cortical (CSTC) circuit, which has been hypothesised to lead to non-motor symptoms
34 such as depression. Individuals with PD have both lower synaptic density and changes in neuronal
35 metabolic function in the basal ganglia, as measured using [¹¹C]UCB-J and [¹⁸F]FDG positron
36 emission tomography (PET), respectively. However, the two radioligands have not been directly
37 compared in the same PD subject or in neurodegeneration animal models. Here, we investigate
38 [¹¹C]UCB-J binding and [¹⁸F]FDG uptake in the CSTC circuit following a unilateral dopaminergic
39 lesion in rats and compare it to sham lesioned rats.

40 Rats received either a unilateral injection of 6-hydroxydopamine (6-OHDA) or saline in the medial
41 forebrain bundle and rostral substantia nigra (n=4/group). After three weeks, all rats underwent two
42 PET scans using [¹⁸F]FDG, followed by [¹¹C]UCB-J on a separate day. [¹⁸F]FDG uptake and
43 [¹¹C]UCB-J binding were both lower in the ipsilateral striatal regions compared to the contralateral
44 regions. Using [¹¹C]UCB-J, we could detect an 8.7% decrease in the ipsilateral ventral midbrain,
45 compared to a 2.9% decrease in ventral midbrain using [¹⁸F]FDG. Differential changes between
46 hemispheres for [¹¹C]UCB-J and [¹⁸F]FDG outcomes were also evident in the CSTC circuit's
47 cortical regions, especially in the orbitofrontal cortex and medial prefrontal cortex where higher
48 synaptic density yet lower neuronal metabolic function was observed, following lesioning.

49 In conclusion, [¹¹C]UCB-J and [¹⁸F]FDG PET can detect divergent changes following a
50 dopaminergic lesion in rats, especially in cortical regions that are not directly affected by the
51 neurotoxin. These results suggest that combined [¹¹C]UCB-J and [¹⁸F]FDG scans could yield a
52 better picture of the heterogeneous cerebral changes in neurodegenerative disorders.

53 1 Introduction

54 Several techniques have been developed to identify disease-related neuronal patterns to aid early
55 detection and differential diagnoses of Parkinson's disease (PD). Examples of such methods are
56 positron emission tomography (PET) imaging to measure glucose metabolism (Loane and Politis,
57 2011), dopamine synthesis, transporters, or receptors (Kerstens and Varrone, 2020). In PD, one
58 affected neuronal circuit is the cortico-striato-thalamo-cortical (CSTC) circuit (Vriend et al., 2014).
59 The CSTC circuit connects the cortex with the basal ganglia to control and coordinate goal-directed
60 behaviour. This circuit can be further divided into three loops: the motor, limbic, and associative
61 circuits (Groenewegen and Trimble, 2007; Vriend et al., 2014). The dopamine system innervates the
62 striatal regions of the CSTC circuits and is critical in modulating their output. A model of 6-
63 hydroxydopamine (6-OHDA) induced dopaminergic lesion leads to modulation within the CSTC,
64 which will further help understand this circuit (Schwarting and Huston, 1996).

65 [¹¹C]UCB-J is a PET radioligand showing high affinity to synaptic vesicle glycoprotein 2A (SV2A)
66 (Nabulsi et al., 2016). SV2A is ubiquitously expressed throughout the brain (Bajjalieh et al., 1994;
67 Südhof, 2004) and is a suitable proxy for synaptic density (Finnema et al., 2016). Accordingly,
68 [¹¹C]UCB-J PET may serve as a biomarker in neurodegenerative disorders, where the loss of
69 synapses is thought to play a vital role in the pathophysiology (Holland et al., 2020; Matuskey et al.,
70 2020; Mecca et al., 2020; Nicastro et al., 2020; Wilson et al., 2020; O'Dell et al., 2021).
71 [¹⁸F]fluorodeoxyglucose (FDG) is a glucose analogue used to measure neuronal glucose consumption

72 and metabolic function. [¹⁸F]FDG PET has also been used as a surrogate marker for neuronal
73 integrity and function (Mosconi, 2013). Only very recently, [¹⁸F]FDG and [¹¹C]UCB-J were tested in
74 the same Alzheimer patients (Chen et al., 2021), where [¹¹C]UCB-J proved valuable as a clinical
75 tracer and marker for disease progression, which may be helpful in drug development. This
76 combination of radioligands has not been tested in human PD subjects or animal models of
77 neurodegeneration.

78 Here we present a multimodal PET study using dynamic [¹¹C]UCB-J and static [¹⁸F]FDG scans in
79 the rat model of 6-OHDA severe unilateral-dopaminergic lesioning induced by combined unilateral
80 6-OHDA injection in the medial forebrain bundle and rostral substantia nigra (Yuan et al., 2005;
81 Blandini et al., 2008). We have previously shown that 6-OHDA lesioning lowers postsynaptic
82 dopamine receptor density and presynaptic capacity to release amphetamine (Palner et al., 2011).
83 Thus, we hypothesise that the loss of dopaminergic neurons will cause a decrease in [¹¹C]UCB-J
84 binding and [¹⁸F]FDG uptake, especially in the ipsilateral basal ganglia (substantia nigra, ventral
85 tegmental area, whole striatum, dorsolateral striatum, dorsomedial striatum, and nucleus accumbens).
86 Furthermore, we compare the effect sizes of [¹⁸F]FDG uptake and [¹¹C]UCB-J binding to detect
87 changes after a unilateral dopaminergic lesioning of the rat brain. As a control to assess differential
88 changes, we used both the contralateral hemisphere and compared the 6-OHDA model to a group of
89 sham-lesioned rats. Several studies have successfully detected changes in regional [¹⁸F]FDG uptake
90 after a 6-OHDA lesion in both rats (Casteels et al., 2008; Jang et al., 2012; Silva et al., 2013; Kordys
91 et al., 2017) and mice (Im et al., 2016). One recent study has also performed [¹¹C]UCB-J PET in the
92 6-OHDA lesion model, although with some methodological differences (Thomsen et al., 2021b).

93 The results of our study indicate that dopaminergic lesions lead to a loss of presynaptic density in the
94 striatal regions, as measured by [¹¹C]UCB-J, which is similar to changes in neuronal metabolic
95 function, as measured by [¹⁸F]FDG. Interestingly, the dopaminergic lesion caused divergent changes
96 between the two radioligands in cortical regions of the CSTC circuit.

97 2 Materials and Methods

98 2.1 Animals:

99 Eight female Long-Evans WT rats (239 ± 12 g, 10-11 weeks old when scanned) (Janvier) were used
100 in this study. The animals were held under standard laboratory conditions with 12-hour light/12-hour
101 dark cycles and ad libitum access to food and water. All animal experiments conformed to the
102 European Commission's Directive 2010/63/EU with approval from the Danish Council of Animal
103 Ethics (Journal no. 2017-15-0201-01375) and the Department of Experimental Medicine, University
104 of Copenhagen.

105 2.2 Stereotactic surgery and 6-OHDA lesion:

106 The animals were acclimatised in the surgery room for at least 1 hour. Analgesia was provided with
107 carprofen (Rimadyl, Zoetis, NJ, USA) 5 mg/kg, subcutaneous (SC), 45 minutes before the surgery
108 and 24 hours and 48 hours postoperative. Before commencing the surgery, animals received
109 desmethylimipramine (25 mg/kg, intraperitoneal (IP)) mixed in physiological saline.
110 Desmethylimipramine protects the noradrenergic neurons from the neurotoxic effects (Esteban et al.,
111 1999). Anaesthesia was induced with 3% isoflurane in oxygen and maintained through surgery with
112 1.2-1.8% isoflurane in oxygen. The rats were fixed on a stereotaxic apparatus (Kopf Instruments,
113 Tujunga, CA, USA) with the incisor bar set 3.3 mm below the level of the ear bars. An incision was
114 made on the scalp, and two bur-holes were drilled on one side of the skull using a dental micromotor

115 and round bur (0.5 mm). A 2 μ g/ μ L solution of 6-OHDA (2,5-Dihydroxytyramine hydrobromide, Sigma-Aldrich, Søborg, Denmark) in physiological saline containing 0.02% ascorbic acid or physiological saline (containing 0.02% ascorbic acid) was drawn into a 10 μ L syringe with a 33 g needle (World Precision Instruments, Sarasota, FL, USA). 3 μ L were infused into the medial forebrain bundle (coordinates: AP= 4.8 mm, ML= 1.7 mm, DV= 8 mm) and 3 μ L infused rostral to substantia nigra (coordinates: AP= 3.6 mm, ML= 2 mm, DV= 8.3 mm) relative to the bregma to ensure unilateral dopaminergic degeneration. The infusion was delivered at 151 nL/minutes driven by an infusion pump (World Precision Instruments, Sarasota, FL, USA), followed by a 7 minute pause prior to a slow withdrawal of the syringe needle. The incision was sutured back. After recovery from anaesthesia, rats were returned to the recovery cage and housed alone for 48 hours and then housed in pairs for recovery of 21 days to allow the development of the lesions.

126 **2.3 Study design and confirmation of lesion:**

127 Four rats were injected unilaterally with 6-OHDA, while another four were injected with 128 physiological saline and divided into two groups, i.e., dopamine lesioned and sham lesioned; Figure 1 129 shows the study's overall design. After the recovery period, the rats were subjected to two PET scans 130 [¹⁸F]FDG at day 21 and [¹¹C]UCB-J at approximately day 23. One month (26-33 days) after the 131 injection, the rats were euthanised by decapitation, and the brains rapidly removed and frozen on dry 132 ice.

133 To validate the extent of the lesion, tyrosine hydroxylase (TH) immunostaining was performed on 20 134 μ m coronal cryosections containing the striatum. Frozen brains were sectioned on a cryostat (Leica 135 CM1800, Leica Biosystems, Buffalo Grove, IL, USA) and mounted on Superfrost Plus™ adhesion 136 microscope slides (Thermo Fischer Scientific, MS, USA). Sections were stored at -80°C for the 137 remaining period of the study. The sections were dried and processed for standard TH 138 immunohistochemistry. Briefly, the frozen sections were first fixed in cold (4°C) 4% formaldehyde 139 for 15 minutes. The sections were then prewashed in 0.05 M phosphate-buffered saline (PBS, pH 140 7.4) with 1% bovine serum albumin and then incubated overnight in a purified antiserum against TH 141 generated in rabbits (Sigma-Aldrich, Søborg, Denmark; cat#AB152) diluted 1:500 in PBS + 0.1% 142 Triton-X overnight at 4°C. The immunoreactivity was detected using the avidin-biotin detection 143 method (biotinylated donkey-anti rabbit IgG (Sigma-Aldrich, Søborg, Denmark, #SAB3700966); 144 avidin-biotin-peroxidase complex (Thermo Fischer Scientific, MS, USA #32020)) and reacted for 145 peroxidase activity in 0.1% diamino-benzidine mixed with 0.003% H₂O₂ in PBS for 15 minutes. 146 Finally, the sections were washed in distilled water and embedded in Pertex.

147 The stained slides were imaged on a Zeiss Axio Observer 7 using an EC Plan-Neofluor 5x/0.16 148 objective by stitching multiple fields of view to cover the entire section. The resulting colour image 149 was analysed in ImageJ 1.53G (NIH Image, Bethesda, MD, USA) by a workflow involving masking 150 potential artefacts by automatic threshold (Moment) and conversion to 16-bit grayscale. From these, 151 crude regions of interest encompassing the striatum were identified for quantification. Automated 152 thresholds were used to measure the intensities in mean grey values (Minimum) and stained areas in 153 pixel values (Moment). The intensities and areas of the ipsilateral striatum were normalised to the 154 contralateral striatum and are presented as percentages.

155 **2.4 [¹⁸F]FDG and [¹¹C]UCB-J PET scans:**

156 All scans were performed on the Siemens HRRT (High-Resolution Research Tomography), and all 157 rats were examined using both [¹¹C]UCB-J and [¹⁸F]FDG. The rats were transported to the scanner at 158 least 2 hours before the scan. Anaesthesia was induced using 3% isoflurane in oxygen. All rats were

159 placed in a 2 x 2 custom made rat holder (illustration in Figure 1), enabling simultaneous scanning of
160 four rats (Keller et al., 2017; Shalgunov et al., 2020; Casado-Sainz et al., 2021). While in the custom-
161 made rat holder, the rats were kept under anaesthesia with a constant flow of isoflurane (~2%
162 isoflurane in oxygen). They were placed in the HRRT scanner for the time of the scan. The rats were
163 kept warm using an infrared lamp and monitored for respiration throughout the entire scan. A
164 rotating point source ¹³⁷Cs transmission scan (Keller et al., 2013) was carried out before or after each
165 emission scan.

166 [¹⁸F]FDG was acquired from the in-house clinical production of the department of clinical
167 physiology, nuclear medicine and PET, Rigshospitalet, Denmark. Rats were fasted overnight before
168 the scan. The animals were briefly anaesthetised, and [¹⁸F]FDG was administered intraperitoneal
169 with an average injected dose of 25.05 ± 3.1 MBq. The rats were placed back in their home cage to
170 wake up from the anaesthesia to achieve [¹⁸F]FDG uptake while awake. Forty-five minutes after the
171 [¹⁸F]FDG injection, the rats were anaesthetised, placed in the holder, and a PET emission scan was
172 acquired for 45 minutes.

173 [¹¹C]UCB-J was produced in-house using a modified protocol (see supplementary information)
174 adapted from Nabulsi et al. (Nabulsi et al., 2016). The tail veins were canulated (BD Neoflon 25G,
175 Stockholm, Sweden) before the scan. At the start of the scan, intravenous (IV) injections were given
176 over 7-10 seconds through the tail vein catheter, with an average dose of 20.8 ± 2.1 MBq (injected
177 mass = 0.04 ± 0.01 µg). Heparinised saline (500-600 µL) was flushed through the catheter after tracer
178 injection. The acquisition time for [¹¹C]UCB-J was 60 minutes.

179 **2.5 PET image reconstruction:**

180 All list-mode data was dynamically reconstructed using ordinary Poisson 3D ordered subset
181 expectation maximisation with point spread function modelling, resulting in PET image frames
182 consisting of 207 planes of 256 x 256 voxels (1.22 x 1.22 x 1.22 mm). The reconstruction of the
183 attenuation map from the transmission scan was performed using the maximum a posteriori
184 algorithm for transmission data. All [¹¹C]UCB-J scans were transformed into 33 dynamic frames (6 x
185 10, 6 x 20, 6 x 60, 8 x 120 and 7 x 300 seconds), while [¹⁸F]FDG scans were transformed into 5-
186 minute frames and then averaged into a single frame.

187 **2.6 Quantification of PET data:**

188 Pre-processing of all PET scans were done with PMOD 3.7 (PMOD Technologies, Zürich,
189 Switzerland). Kinetic modelling was done with PMOD 3.0 (PMOD Technologies, Zürich,
190 Switzerland). All rats were scanned in full-body, and brains were manually cropped out. For
191 [¹⁸F]FDG scans, static images were manually co-registered to a standard [¹⁸F]FDG PET template.
192 For [¹¹C]UCB-J scans, a summed image of the last 13 frames were manually co-registered to an
193 average T1-weighted magnetic resonance brain image in standard space. MR template used was a
194 summed image from various rats, not part of this study, generously provided by Kristian Nygaard
195 Mortensen. Volumes of interest (VOIs)-atlas of selected regions from the CSTC circuit from
196 Schiffer's atlas (Schiffer et al., 2006) were applied to the PET image in standard space. The regions
197 (depicted in Figure 3 and Supplementary Figure 4) included in this study were: anterior cingulate
198 cortex, medial prefrontal cortex, motor cortex, nucleus accumbens, orbitofrontal cortex, striatum,
199 thalamus, and ventral midbrain (a region covering both the ventral tegmental area and substantia
200 nigra). The dorsomedial striatum and dorsolateral striatum were manually delineated and used in the
201 study (Shalgunov et al., 2020; Casado-Sainz et al., 2021). All images and co-registration were
202 visually checked for accuracy following spatial transformation.

203 For [¹⁸F]FDG, the unit of measurement (Bq/mL) for each cropped image was transformed into
204 standardised uptake values (SUV) by adjusting for body weight and injected dose. A whole-brain
205 normalisation factor (WB_{nf}) was calculated for each rat using [Eq. 1]. The SUV values from all the
206 VOIs were normalised using WB_{nf}.

207

208
$$WB_{NF} = \frac{\text{Average of whole-brain } [{}^{18}\text{F}]FDG \text{ SUV for all rats}}{\text{Whole-brain } [{}^{18}\text{F}]FDG \text{ SUV for rat X}} \quad [\text{Eq. 1}]$$

209

210 For [¹¹C]UCB-J, time-activity curves (TACs) for all VOIs were extracted from the PET images.
211 Estimates for the total blood activity was acquired using a non-invasive image-derived input function
212 (IDIF) that was used for estimating a surrogate of V_T. V_T was determined in each VOI, using the
213 one-tissue compartment model (1TCM), which has previously been validated for [¹¹C]UCB-J in mice
214 (Bertoglio et al., 2020; Xiong et al., 2021). The IDIF was extracted from each PET image by
215 delineating the whole blood activity in the lumen of the heart's left ventricle. This delineation was
216 achieved by using the 'region growing' function in PMOD in the early time frame by dropping a
217 'seed' at the point of highest activity in the heart and producing a VOI which is about the size of the
218 rat's left ventricle (5-6 voxels). In order to fit the 1TCM to the TACs, the blood volume fraction (V_B)
219 was fixed at 5%. In addition to V_T, the micro-parameters K₁ and k₂ were also extracted from the
220 kinetic modelling. These micro-parameters were checked for the difference due to the surgical
221 procedure or any other reason. 1TC model fit to a representative region, ipsilateral and contralateral
222 striatum, are shown in Supplementary Figure 5. All micro parameters (K1 and k2) for all regions are
223 recorded in Supplementary Table 2. In addition to kinetic modelling, TACs were converted into
224 SUVs. Ipsilateral and contralateral striatum and ventral midbrain (sham and dopamine lesioned)
225 TACs were averaged for visual representation. This was performed using GraphPad Prism 9
226 (GraphPad Software, San Diego, CA, USA).

227 **2.7 Statistics:**

228 Due to the limited sample size and the number of comparisons undertaken, the study is exploratory in
229 nature, meaning that caution should be taken around drawing strong confirmatory conclusions from
230 the data. As such, all p-values reported should be considered as a continuous assessment of indirect
231 evidence against the null hypothesis of no difference between groups or hemispheres, and binary
232 conclusions of "significant" or "not significant" within the Neyman-Pearson Null-hypothesis-
233 significance-testing framework should be avoided.

234 The data were analysed using Jamovi (Version 1.6, The jamovi project (2021) [Computer Software].
235 Retrieved from <https://www.jamovi.org>) and RStudio (v. 4.0.3; "Bunny-Wunnies Freak Out", R core
236 team, Vienna, Austria). Graph-Pad Prism (v. 9.0.1; GraphPad Software, San Diego, CA, USA) was
237 used for data visualisation. All data are presented as mean values \pm standard deviation unless
238 otherwise specified. The TH immunostaining comparison of the dopamine and sham lesion
239 (ipsilateral side corrected to the contralateral side) was performed with an independent samples t-test
240 (Mann-Whitney test).

241 To allow direct comparison of [¹⁸F]FDG normalised SUVs and [¹¹C]UCB-J V_T, Cohen's dz values (a
242 standardised measure of within-subject differences) between the ipsilateral regions and contralateral
243 regions were calculated (Lakens, 2013). Cohen's dz (standardised measure of between-group

244 differences) values were used to compare the effect size measured by the two tracers. This shows the
245 efficacy of detecting differences with the two radioligands.

246 To further explore and compare the different regions, the difference between the ipsilateral and
247 contralateral side for each tracer (¹⁸F]FDG and ¹¹C]UCB-J) in the dopamine and sham lesioned
248 groups was calculated in Jamovi using paired t-test without correction for multiple comparisons.

249 We performed tests on ¹⁸F]FDG normalised SUVs and ¹¹C]UCB-J V_T between the two lesioned
250 groups in regions outside the basal ganglia: thalamus, medial prefrontal cortex, anterior cingulate
251 cortex, orbitofrontal cortex and motor cortex. These tests were performed using an independent
252 samples t-test (Mann-Whitney test).

253 3 Results

254 3.1 Confirmation of lesion

255 Striatal TH immunostaining confirmed unilateral dopaminergic lesions in the striatum (Figure 2). We
256 observed a 73.9% decrease (p = 0.03) in the stained area from the sham lesioned animals (97.50% ±
257 6.77) to the dopamine lesioned animals (23.54% ± 9.41). These observations were accompanied by a
258 24.68% reduction in staining intensity (p= 0.03) between sham lesioned (93.39% ± 4.73) and
259 dopamine lesioned animals (68.72% ± 6.62).

260 3.2 Representative ¹¹C]UCB-J and ¹⁸F]FDG PET images

261 Representative ¹¹C]UCB-J and ¹⁸F]FDG PET images from a rat in the dopamine and sham lesioned
262 group are shown in Figure 3. A template structural T1 MR image is used for illustrative purpose
263 only. Regional VOIs are shown on summed PET images in Supplementary Figure 4. For ¹¹C]UCB-
264 J, a difference was visually noticed between the ipsilateral and contralateral side of the 6-OHDA
265 injection, especially in the striatal regions and ventral midbrain (red arrows in Figure 3). Hemispheric
266 differences were not evident in the sham lesioned animal. For ¹⁸F]FDG, changes were also evident
267 between the ipsilateral and contralateral hemisphere in the cortex, striatal regions, and ventral
268 midbrain in the dopamine lesioned animal (red arrows in Figure 3), while no apparent differences
269 were seen in the sham lesioned animal.

270 3.3 Decreased ¹¹C]UCB-J V_T in dopamine lesioned hemisphere

271 Visually, a lower average ¹¹C]UCB-J uptake can be seen through averaged TACs in the ipsilateral
272 striatum and ventral midbrain compared to the contralateral hemisphere in dopamine lesioned
273 animals (Figure 4 A and B). No changes were noticed in the sham lesioned animals (Figure 4 C and
274 D). ¹¹C]UCB-J V_T values were lower in the ipsilateral side of the striatum, dorsolateral striatum and
275 ventral midbrain but higher in the medial prefrontal cortex and anterior cingulate cortex compared to
276 the contralateral side (Figure 4 E and Table 1). In the sham lesioned animals, higher ¹¹C]UCB-J V_T
277 values were also seen in the ipsilateral anterior cingulate cortex compared to the contralateral side.
278 No other differences were observed in ¹¹C]UCB-J V_T (Figure 4 F and Table 1) between the
279 ipsilateral and contralateral sides in the sham lesioned rats.

280 3.4 Decreased ¹⁸F]FDG uptake in dopamine lesioned hemisphere

281 There was a lower uptake of ¹⁸F]FDG in all striatal regions (only statistically significant in
282 dorsolateral striatum), thalamus and orbitofrontal cortex in the ipsilateral side of dopamine lesioned

283 rats, compared to the contralateral side (Figure 5 and Table 1). No substantial differences were found
284 between the ipsilateral and contralateral sides within the sham lesioned animals.

285 **3.5 [¹¹C]UCB-J and [¹⁸F]FDG show divergent effect sizes in dopamine and sham lesioned
286 animals**

287 Both [¹¹C]UCB-J and [¹⁸F]FDG show an expected negative effect of the dopaminergic lesion in all
288 dopamine rich regions, including the ventral midbrain, striatum, dorsomedial striatum, dorsolateral
289 striatum and nucleus accumbens (Figure 6). Results are reported as Cohen's dz values, showing the
290 within-subject effect size between the ipsilateral and contralateral hemispheres. The ventral midbrain
291 and striatum show a larger effect with [¹¹C]UCB-J than [¹⁸F]FDG, although with confidence intervals
292 overlapping the mean of the other radioligand. The dorsomedial striatum, dorsolateral striatum and
293 nucleus accumbens also have overlapping confidence intervals and shows a similar effect with
294 [¹¹C]UCB-J or [¹⁸F]FDG.

295 Besides dopamine rich regions, there is a seemingly larger reduction with [¹⁸F]FDG compared to
296 [¹¹C]UCB-J in the thalamus; however, the [¹⁸F]FDG confidence interval still includes the mean of
297 [¹¹C]UCB-J. Divergent changes can be seen in cortical regions when comparing [¹¹C]UCB-J and
298 [¹⁸F]FDG except for the motor cortex, which shows no effect of the dopamine lesion. In particular,
299 the medial prefrontal cortex and orbitofrontal cortex shows a negative effect with [¹⁸F]FDG (higher
300 SUV on the lesioned side), while it shows a positive effect with [¹¹C]UCB-J (lower V_T on the
301 lesioned side). The anterior cingulate cortex shows no effect with [¹⁸F]FDG but a positive effect with
302 [¹¹C]UCB-J. Sham lesioned animals do not show differences between hemispheres, except for
303 [¹¹C]UCB-J in the anterior cingulate cortex.

304 **3.6 Changes in cortical regions between [¹¹C]UCB-J binding and [¹⁸F]FDG uptake**

305 A post hoc analysis of changes in the cortical regions and thalamus between the lesion and sham
306 group (Figure 7) showed an increase in [¹¹C]UCB-J V_T values in the anterior cingulate cortex
307 (37.36%, p = 0.03) whereas there is no difference in [¹⁸F]FDG uptake (2.6%, p = 0.68). On the
308 contrary, a lower [¹⁸F]FDG uptake is observed in the motor cortex (-16.42%, p = 0.03) and the
309 orbitofrontal cortex (-11.08%, p = 0.03), which is not the case for [¹¹C]UCB-J V_T (16.8%, p = 0.34
310 and 19.8%, p = 0.20).

311 **4 Discussion**

312 This study explored regional differences in [¹¹C]UCB-J binding and [¹⁸F]FDG uptake using a
313 unilateral 6-OHDA dopaminergic lesion in rats, a commonly used animal model for PD. We
314 observed differences in SV2A density and neuronal metabolic function between ipsilateral and
315 contralateral hemispheres, especially the basal ganglia, which are well known to be innervated by
316 dopaminergic terminals. This suggests a decline in dopaminergic neurons and synapses due to the 6-
317 OHDA lesion, consistent with TH immunostaining (Figure 2).

318 We derived effect sizes between the ipsilateral and contralateral regions to directly compare
319 [¹¹C]UCB-J and [¹⁸F]FDG. The regions within the basal ganglia show similar effects with the two
320 radioligands, lower SV2A density and metabolic function, in the ipsilateral region compared to the
321 contralateral region. Especially lower SV2A density in the striatum, dorsolateral striatum, and ventral
322 midbrain compared to the contralateral regions. We see a strong correlation between in vitro
323 autoradiography (³H]UCB-J fmol/mg tissue equivalent) and PET quantification ([¹¹C]UCB-J V_T) in
324 the sham lesioned animal (Supplementary data 1.2). This further confirms the validity of the

325 [¹¹C]UCB-J PET data. A lower ipsilateral metabolic function is also observed in the regions of basal
326 ganglia, which is consistent with previous 6-OHDA lesion studies showing an ipsilateral decrease in
327 [¹⁸F]FDG uptake in the striatal regions compared to the contralateral regions (Casteels et al., 2008;
328 Jang et al., 2012; Kordys et al., 2017). No such changes are evident in baseline animals
329 (Supplementary data 1.1). Our observations are in line with the common understanding of the CSTC
330 circuitry, in which the striatal response is in part sculptured by the dopaminergic input from
331 substantia nigra (Vriend et al., 2014). Hence, diminished activity in dopamine neurons projecting to
332 the striatum due to the 6-OHDA lesion would lead to a decline in striatal activity, as is evident from
333 the changes in [¹⁸F]FDG uptake.

334 A difference of moderate magnitude between the ipsilateral and contralateral thalamus was noted for
335 [¹⁸F]FDG but not for [¹¹C]UCB-J. Although dopamine denervation of the rodent thalamus is scant
336 (Papadopoulos and Parnavelas, 1990), we still observe decreased metabolic function. This may be
337 due to the overall decreased function of the lesioned thalamus.

338 The cortical regions also show divergent group differences with [¹¹C]UCB-J and [¹⁸F]FDG. In the
339 orbitofrontal cortex and medial prefrontal cortex, [¹⁸F]FDG uptake is lower in the ipsilateral regions
340 compared to contralateral regions. By contrast, [¹¹C]UCB-J shows higher SV2A density in the
341 ipsilateral regions compared to the contralateral regions. To our knowledge, it is the first time that a
342 lower orbitofrontal cortex metabolic function is demonstrated in this rat model; a decrease has
343 previously only been reported in the prefrontal cortex (Casteels et al., 2008), while other studies
344 show unaltered metabolism (Kurachi et al., 1995). The decrease in orbitofrontal and medial
345 prefrontal cortical metabolic function may be due to the disrupted dopaminergic innervation from the
346 substantia nigra to the orbitofrontal cortex (Murphy and Deutch, 2018).

347 [¹¹C]UCB-J binding is higher in the anterior cingulate cortex in most of the tests that we perform,
348 except baseline animals (Supplementary data 1.1). While showing no effect in metabolic function,
349 the anterior cingulate cortex's SV2A density was higher ipsilaterally, both in the sham and dopamine
350 lesioned animals. Likewise, the anterior cingulate cortex had higher SV2A density in the dopamine
351 lesioned animals than sham lesioned animals, both in ipsilateral (Figure 7) and contralateral
352 hemispheres (Supplementary Figure 3). These changes are also evident in vitro using [³H]UCB-J
353 autoradiography (Supplementary data 1.2) in the sham lesioned animals (Supplementary Figure 2).
354 Such changes in the cingulate cortex have not been previously shown in this model. We speculate
355 that the cause is the surgery itself as the anterior cingulate cortex is part of the pain matrix (Bliss et
356 al., 2016), but further testing is necessary to understand this observation. In addition, a reduced
357 mechanical nociceptive threshold has been extensively reported in the 6-OHDA model, which maybe
358 is directly related to changes in synaptic density in the anterior cingulate cortex (Buhidma et al.,
359 2020).

360 We observed a lower metabolic function in the ipsilateral motor cortex and the orbitofrontal cortex
361 between the 6-OHDA-injected and saline-injected cortices. The difference in the motor cortex is also
362 seen in patients with PD, but reduced metabolic function in the orbitofrontal cortex are not
363 commonly seen in PD subjects (Meyer et al., 2017). Such cortical reduction was not detected with
364 [¹¹C]UCB-J, implying the relative robustness in detecting circuit changes with [¹⁸F]FDG.

365 Disease-specific changes in SV2A density, i.e. synaptic loss, have now been demonstrated in rodent
366 models of neurodegeneration with intracranial injections of neurotoxic agents or with protein
367 inoculation models of PD (Thomsen et al., 2021b, 2021a). Such synaptic loss is also demonstrated in
368 other Alzheimer's disease and PD mice models (Toyonaga et al., 2019; Xiong et al., 2021). Our

369 study supports the recent study's findings with lower SV2A density within the basal ganglia in the 6-
370 OHDA rat model (Thomsen et al., 2021b), although there are methodological differences, such as
371 employing different kinetic models and site of injection.

372 [¹¹C]UCB-J has now been used in monkeys(Nabulsi et al., 2016), pigs(Thomsen et al., 2020),
373 mice(Bertoglio et al., 2020), rats(Thomsen et al., 2021b) and humans(Finnema et al., 2016) and show
374 favourable brain penetration, fast uptake and acceptable washout kinetics. In rats and mice, various
375 kinetic modelling was performed using an arterial blood sampling scheme or image-derived input
376 function (IDIF) from the heart (Bertoglio et al., 2020; Glorie et al., 2020; Thomsen et al., 2021b).
377 The 1TCM and 2TCM both work favourably with [¹¹C]UCB-J using the heart as an IDIF (Bertoglio
378 et al., 2020; Glorie et al., 2020). The use of IDIF and whole-brain normalisation allows longitudinal
379 studies in rodents since blood sampling often is laborious and error-prone. Although most of these
380 studies are using mice, we assume it translates well to rats.

381 The small sample size is a limitation of our study, making it particularly hard to conclude that there
382 are no differences (type 2 error). For that reason, we took an exploratory approach without pre-
383 registered predictions and without corrections for multiple testing. As such, the results should be seen
384 as preliminary, and we caution against confirmatory conclusions from the results and encourage
385 future replications using larger samples and a more limited selection of analyses. Further, the
386 contralateral hemisphere may not be an ideal control region because of the inter-hemisphere
387 anatomical connection of the basal ganglia through the pedunculopontine nucleus (Breit et al., 2008).
388 [¹⁸F]FDG results must be evaluated with caution. Other factors, such as neuroinflammation due to the
389 injection or lesion, could evoke increased regional glucose consumption, thus concealing a decreased
390 neuronal function (Blandini et al., 2008). Crabbé et al. have shown an increase in P2X7 receptor (key
391 mediator in neuroinflammation), as well as translocator protein (TSPO) in 6-OHDA, lesioned
392 animals compared to sham lesioned animals using autoradiography (Crabbé et al., 2019). These
393 changes were significant at 21 days; hence uptake of [¹⁸F]FDG in the ventral midbrain may be due to
394 neuroinflammation, which is hard to differentiate using [¹⁸F]FDG. Our setup in a clinical high-
395 resolution PET scanner allows for simultaneous scanning of up to four rats, which further allowed us
396 to perform four [¹¹C]scans with a single radiosynthesis. Although this saves resources and enables a
397 more direct comparison between rats, the resolution of the HRRT is lower than other available
398 single-subject small animal micro-PET systems. Hence, our ability to identify potentially apparent
399 biological differences in small regions is limited due to, e.g., partial volume effects.

400 Regardless, we found a pattern in the regional cortical synaptic density and neuronal metabolic
401 function, which could be clinically relevant, especially changes within the anterior cingulate cortex
402 and orbitofrontal cortex. We see a clear advantage of including both tracers to get a clearer picture of
403 the neuropathology of neurodegenerative diseases like PD.

404 5 Conclusion

405 [¹¹C]UCB-J and [¹⁸F]FDG PET revealed similar changes in the basal ganglia following 6-OHDA
406 dopaminergic lesion in rats. A region-based analysis suggested a divergent response to lesions,
407 especially in the cortical regions, orbitofrontal cortex and medial prefrontal cortex, where higher
408 synaptic density yet lower neuronal metabolic function was observed. Taken together, the results
409 suggest that combined [¹¹C]UCB-J and [¹⁸F]FDG scans may yield a better understanding of aberrant
410 CSTC circuit function and a better diagnostic outcome in patients with neurodegenerative disorders.

411 6 Conflict of Interest

412 MP: Compass Pathways Plc (research collaboration), GMK: H. Lundbeck A/S (research
413 collaboration), Compas Pathways Plc (research collaboration), Elysis (research collaboration), Novo
414 Nordisk/Novozymes/Chr. Hansen (stockholder), Sage Therapeutics and Sanos (Advisor). GMK is
415 currently the president of the European College of Neuropsychopharmacology. All other authors
416 declare no conflicts of interest.

417 **7 Author Contributions**

418 Conceptualisation, NRR, FG, PPS, MP; methodology, NRR, FG, PPS, MP; software, NRR, FG, PPS,
419 MP; validation, NRR, FG, PPS; formal analysis, NRR, FG, MJ; investigation, NRR, FG, IVA, NRS,
420 AV; resources, NRR, MJ, MP; data curation, NRR, MP; writing—original draft preparation, NRR.;
421 writing—review and editing, NRR, FG, MJ, INP, PPS, GMK, MP; visualisation, NRR; supervision,
422 JM, PMF, MMH, PPS, GMK, MP; funding acquisition, NRR, GMK, MP. All authors have read and
423 agreed to the published version of the manuscript.

424 **8 Funding**



425
426 This project has received funding from the European Union’s Horizon 2020 research and innovation
427 programme under the Marie Skłodowska-Curie grant agreement No 813528. This project also
428 received funding from Parkinson foreningen, Denmark (R16-A247). MP received funding from the
429 Lundbeck Foundation (R192-2015-1591 and R194-2015-1589), Augustinus Foundation (18-3746
430 and 17-1982), Independent Research Fund Denmark (5053-00036B), Savværksejer Jeppe Juhls og
431 Hustrus Ovita Juhls Mindelegat and Købmand i Odense Johann og Hanne Weimann født Seedorffs
432 Legat.

433 **9 Acknowledgements**

434 The authors would like to thank and show sincere gratitude to the veterinarians and staff at the
435 Department of Experimental Medicine, the University of Copenhagen, for their continued assistance
436 with animal experiments. The authors would also like to thank the Department of Clinical
437 Physiology, Nuclear Medicine and PET for their continuous support in imaging. Structural reference
438 rat MR image is generously provided by Kristian Nygaard Mortensen, Center for Translational
439 Neuromedicine, University of Copenhagen.

440 **10 References**

441 Bertoglio, D., Verhaeghe, J., Miranda, A., Kertesz, I., Cybulska, K., Korat, Š., et al. (2020).
442 Validation and non-invasive kinetic modeling of [¹¹C]UCB-J PET imaging in mice. *J. Cereb.
443 Blood Flow Metab.* 40, 1351–1362. doi:10.1177/0271678X19864081.

444 Blandini, F., Armentero, M. T., and Martignoni, E. (2008). The 6-hydroxydopamine model: News
445 from the past. *Park. Relat. Disord.* 14, S124–S129. doi:10.1016/j.parkreldis.2008.04.015.

446 Bliss, T. V. P., Collingridge, G. L., Kaang, B. K., and Zhuo, M. (2016). Synaptic plasticity in the
447 anterior cingulate cortex in acute and chronic pain. *Nat. Rev. Neurosci.* 17, 485–496.
448 doi:10.1038/nrn.2016.68.

449 Breit, S., Martin, A., Lessmann, L., Cerkez, D., Gasser, T., and Schulz, J. B. (2008). Bilateral
450 changes in neuronal activity of the basal ganglia in the unilateral 6-hydroxydopamine rat model.
451 *J. Neurosci. Res.* 86, 1388–1396. doi:10.1002/jnr.21588.

452 Buhidma, Y., Rukavina, K., Chaudhuri, K. R., and Duty, S. (2020). Potential of animal models for
453 advancing the understanding and treatment of pain in Parkinson’s disease. *npj Park. Dis.* 6, 1–7.
454 doi:10.1038/s41531-019-0104-6.

455 Casado-Sainz, A., Gudmundsen, F., Baerentzen, S. L., Lange, D., Ringsted, A., Martinez-Tajada, I.,
456 et al. (2021). Nigro-striatal dopamine activation lowers behavioral and neuronal phenotypes
457 associated with obsessive-compulsive disorder. *bioRxiv*, 2021.02.11.430770.
458 doi:10.1101/2021.02.11.430770.

459 Casteels, C., Lauwers, E., Bormans, G., Baekelandt, V., and Van Laere, K. (2008). Metabolic-
460 dopaminergic mapping of the 6-hydroxydopamine rat model for Parkinson’s disease. *Eur. J.*
461 *Nucl. Med. Mol. Imaging* 35, 124–134. doi:10.1007/s00259-007-0558-3.

462 Crabbé, M., Van Der Perren, A., Bollaerts, I., Kounelis, S., Baekelandt, V., Bormans, G., et al.
463 (2019). Increased P2X7 receptor binding is associated with neuroinflammation in acute but not
464 chronic rodent models for Parkinson’s disease. *Front. Neurosci.* 13.
465 doi:10.3389/fnins.2019.00799.

466 Esteban, S., Lladó, J., Sastre-Coll, A., and García-Sevilla, J. A. (1999). Activation and
467 desensitization by cyclic antidepressant drugs of α 2- autoreceptors, α 2-heteroreceptors and 5-
468 HT(1A)-autoreceptors regulating monoamine synthesis in the rat brain in vivo. *Naunyn.*
469 *Schmiedebergs. Arch. Pharmacol.* 360, 135–143. doi:10.1007/s002109900045.

470 Finnema, S. J., Nabulsi, N. B., Eid, T., Detyniecki, K., Lin, S. F., Chen, M. K., et al. (2016). Imaging
471 synaptic density in the living human brain. *Sci. Transl. Med.* 8.
472 doi:10.1126/scitranslmed.aaf6667.

473 Glorie, D., Verhaeghe, J., Miranda, A., De Lombaerde, S., Stroobants, S., and Staelens, S. (2020).
474 Sapap3 deletion causes dynamic synaptic density abnormalities: a longitudinal [¹¹C]UCB-J
475 PET study in a model of obsessive-compulsive disorder-like behaviour. *EJNMMI Res.* 10.
476 doi:10.1186/s13550-020-00721-2.

477 Jang, D. P., Min, H. K., Lee, S. Y., Kim, I. Y., Park, H. W., Im, Y. H., et al. (2012). Functional
478 neuroimaging of the 6-OHDA lesion rat model of Parkinson’s disease. *Neurosci. Lett.* 513, 187–
479 192. doi:10.1016/j.neulet.2012.02.034.

480 Keller, S. H., L’Estrade, E. N., Dall, B., Palner, M., and Herth, M. (2017). Quantification accuracy of
481 a new HRRT high throughput rat hotel using transmission-based attenuation correction: A
482 phantom study. in *2016 IEEE Nuclear Science Symposium, Medical Imaging Conference and*
483 *Room-Temperature Semiconductor Detector Workshop, NSS/MIC/RTSD 2016* (IEEE), 1–3.
484 doi:10.1109/NSSMIC.2016.8069467.

485 Keller, S. H., Svarer, C., and Sibomana, M. (2013). Attenuation correction for the HRRT PET-
486 scanner using transmission scatter correction and total variation regularization. *IEEE Trans.*
487 *Med. Imaging* 32, 1611–1621. doi:10.1109/TMI.2013.2261313.

488 Kordys, E., Apetz, N., Schneider, K., Duncan, E., Büschbell, B., Rohleder, C., et al. (2017). Motor
489 impairment and compensation in a hemiparkinsonian rat model: correlation between dopamine
490 depletion severity, cerebral metabolism and gait patterns. *EJNMMI Res.* 7. doi:10.1186/s13550-
491 017-0317-9.

492 Kurachi, M., Yasui, S. I., Kurachi, T., Shibata, R., Murata, M., Hagino, H., et al. (1995).
493 Hypofrontality does not occur with 6-hydroxydopamine lesions of the medial prefrontal cortex
494 in rat brain. *Eur. Neuropsychopharmacol.* 5, 63–68. doi:10.1016/0924-977X(94)00136-Y.

495 Lakens, D. (2013). Calculating and reporting effect sizes to facilitate cumulative science: A practical
496 primer for t-tests and ANOVAs. *Front. Psychol.* 4, 863. doi:10.3389/fpsyg.2013.00863.

497 Loane, C., and Politis, M. (2011). Positron emission tomography neuroimaging in Parkinson's
498 disease. *Am. J. Transl. Res.* 3, 323–341. Available at: www.ajtr.org [Accessed March 27, 2021].

499 Meyer, P. T., Frings, L., Rücker, G., and Hellwig, S. (2017). ¹⁸F-FDG PET in Parkinsonism:
500 Differential diagnosis and evaluation of cognitive impairment. *J. Nucl. Med.* 58, 1888–1898.
501 doi:10.2967/jnumed.116.186403.

502 Murphy, M. J. M., and Deutch, A. Y. (2018). Organization of afferents to the orbitofrontal cortex in
503 the rat. *J. Comp. Neurol.* 526, 1498–1526. doi:10.1002/cne.24424.

504 Nabulsi, N. B., Mercier, J., Holden, D., Carr, S., Najafzadeh, S., Vandergeten, M. C., et al. (2016).
505 Synthesis and preclinical evaluation of ¹¹C-UCB-J as a PET tracer for imaging the synaptic
506 vesicle glycoprotein 2A in the brain. *J. Nucl. Med.* 57, 777–784.
507 doi:10.2967/jnumed.115.168179.

508 Papadopoulos, G. C., and Parnavelas, J. G. (1990). Distribution and synaptic organization of
509 dopaminergic axons in the lateral geniculate nucleus of the rat. *J. Comp. Neurol.* 294, 356–361.
510 doi:10.1002/cne.902940305.

511 Schiffer, W. K., Mirrione, M. M., Biegton, A., Alexoff, D. L., Patel, V., and Dewey, S. L. (2006).
512 Serial microPET measures of the metabolic reaction to a microdialysis probe implant. *J.*
513 *Neurosci. Methods* 155, 272–284. doi:10.1016/j.jneumeth.2006.01.027.

514 Shalgunov, V., Xiong, M., L'Estrade, E. T., Raval, N. R., Andersen, I. V., Edgar, F. G., et al. (2020).
515 Blocking of efflux transporters in rats improves translational validation of brain radioligands.
516 *EJNMMI Res.* 10, 124. doi:10.1186/s13550-020-00718-x.

517 Thomsen, M. B., Ferreira, S. A., Schacht, A. C., Jacobsen, J., Simonsen, M., Betzer, C., et al.
518 (2021a). PET imaging reveals early and progressive dopaminergic deficits after intra-striatal
519 injection of preformed alpha-synuclein fibrils in rats. *Neurobiol. Dis.* 149.
520 doi:10.1016/j.nbd.2020.105229.

521 Thomsen, M. B., Jacobsen, J., Lillethorup, T. P., Schacht, A. C., Simonsen, M., Romero-Ramos, M.,
522 et al. (2021b). In vivo imaging of synaptic SV2A protein density in healthy and striatal-lesioned
523 rats with ¹¹C]UCB-J PET. *J. Cereb. Blood Flow Metab.* 41, 819–830.
524 doi:10.1177/0271678X20931140.

525 Thomsen, M. B., Schacht, A. C., Alstrup, A. K. O., Jacobsen, J., Lillethorup, T. P., Bærentzen, S. L.,

526 et al. (2020). Preclinical PET Studies of [¹¹C]UCB-J Binding in Minipig Brain. *Mol. Imaging*
527 *Biol.* 22, 1290–1300. doi:10.1007/s11307-020-01506-8.

528 Toyonaga, T., Smith, L. M., Finnema, S. J., Gallezot, J. D., Naganawa, M., Bini, J., et al. (2019). In
529 vivo synaptic density imaging with ¹¹C-UCB-J detects treatment effects of saracatinib in a
530 mouse model of Alzheimer disease. *J. Nucl. Med.* 60, 1780–1786.
531 doi:10.2967/jnumed.118.223867.

532 Vriend, C., Patti, T., Van Der Werf, Y. D., Voorn, P., Booij, J., Rutten, S., et al. (2014). Depression
533 and impulse control disorders in Parkinson's disease: Two sides of the same coin? *Neurosci.*
534 *Biobehav. Rev.* 38, 60–71. doi:10.1016/j.neubiorev.2013.11.001.

535 Xiong, M., Roshanbin, S., Rokka, J., Schlein, E., Ingelsson, M., Sehlin, D., et al. (2021). In vivo
536 imaging of synaptic density with [¹¹C]UCB-J PET in two mouse models of neurodegenerative
537 disease. *Neuroimage* 239, 118302. doi:10.1016/j.neuroimage.2021.118302.

538

539 11 Data Availability Statement

540 All data is made available at a GitHub repository (<https://github.com/nakulrraval/6-OHDA-rat-PET-paper>). All other requests are directed to the corresponding or first author of this article.
541

542 12 Tables

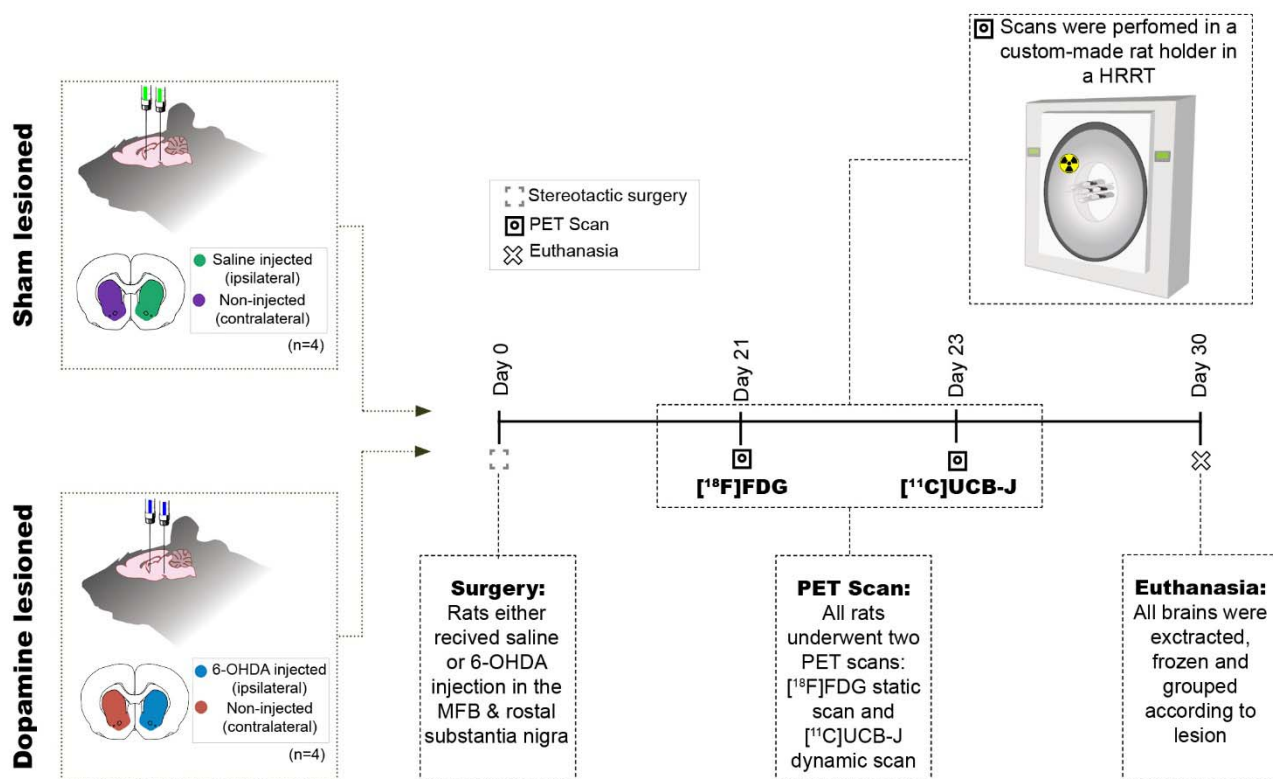
543 **Table 1:** Group-wise summary of the paired t-test between the ipsilateral and contralateral regions
544 for each tracer and group. To aid overview, notable differences are marked as *. Stri= striatum,
545 DMS= dorsomedial striatum, DLS= dorsolateral striatum, NAc= nucleus accumbens, vMB= ventral
546 midbrain, Thal= thalamus, mPFC= medial prefrontal cortex, ACC= anterior cingulate cortex, OFC=
547 orbitofrontal cortex, MoC= motor cortex.

548

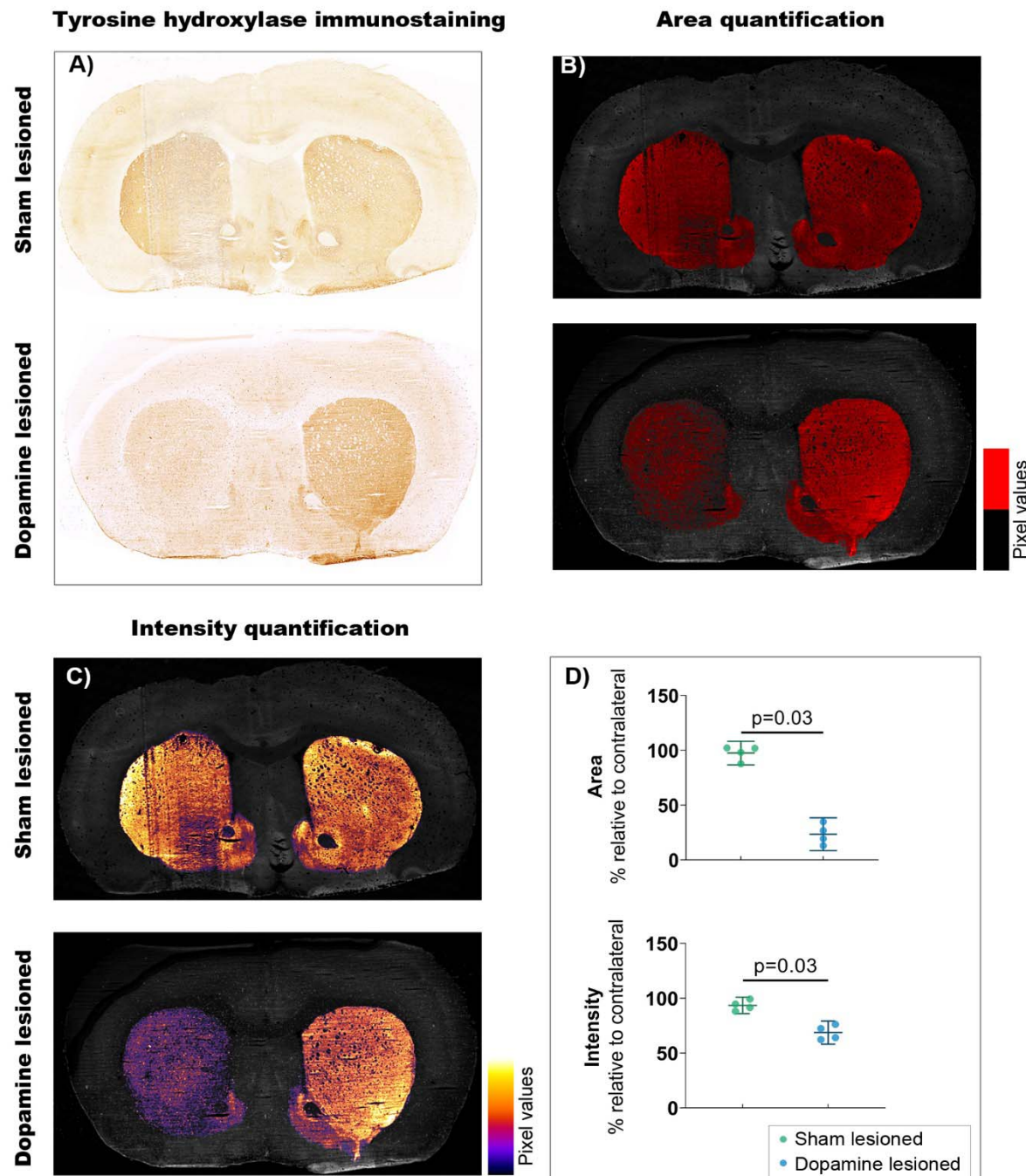
^{[11} C]UCB-J V _T				^{[18} F]FDG Normalized SUVs				
Region	Dopamine Lesioned	Sham Lesioned		Dopamine Lesioned	Sham Lesioned			
	% diff	p value	% diff	p value	% diff	p value	% diff	p value
Stri	-8.86 %	0.003*	-0.99 %	0.66	-5.66 %	0.093	0.25 %	0.926
DMS	-3.48 %	0.085	0.39 %	0.919	-7.42 %	0.077	-1.84 %	0.553
DLS	-5.58 %	0.046*	0.02 %	0.998	-6.30 %	0.022*	-0.45 %	0.893
NAc	-5.35 %	0.122	0.56 %	0.173	-7.26 %	0.071	0.93 %	0.62
vMB	-8.72 %	0.052	3.35 %	0.486	-2.89 %	0.343	0.18 %	0.821
Thal	-2.55 %	0.465	1.20 %	0.233	-4.11 %	0.013*	1.09 %	0.425
mPFC	2.59 %	0.009*	1.33 %	0.621	-2.02 %	0.147	1.25 %	0.47
ACC	2.62 %	0.043*	14.08 %	0.023*	-0.23 %	0.832	0.47 %	0.757
OFC	2.88 %	0.209	5.71 %	0.141	-6.32 %	0.020*	0.45 %	0.67
MoC	1.85 %	0.435	5.27 %	0.169	-1.32 %	0.407	3.25 %	0.223

549

550 13 Figure titles

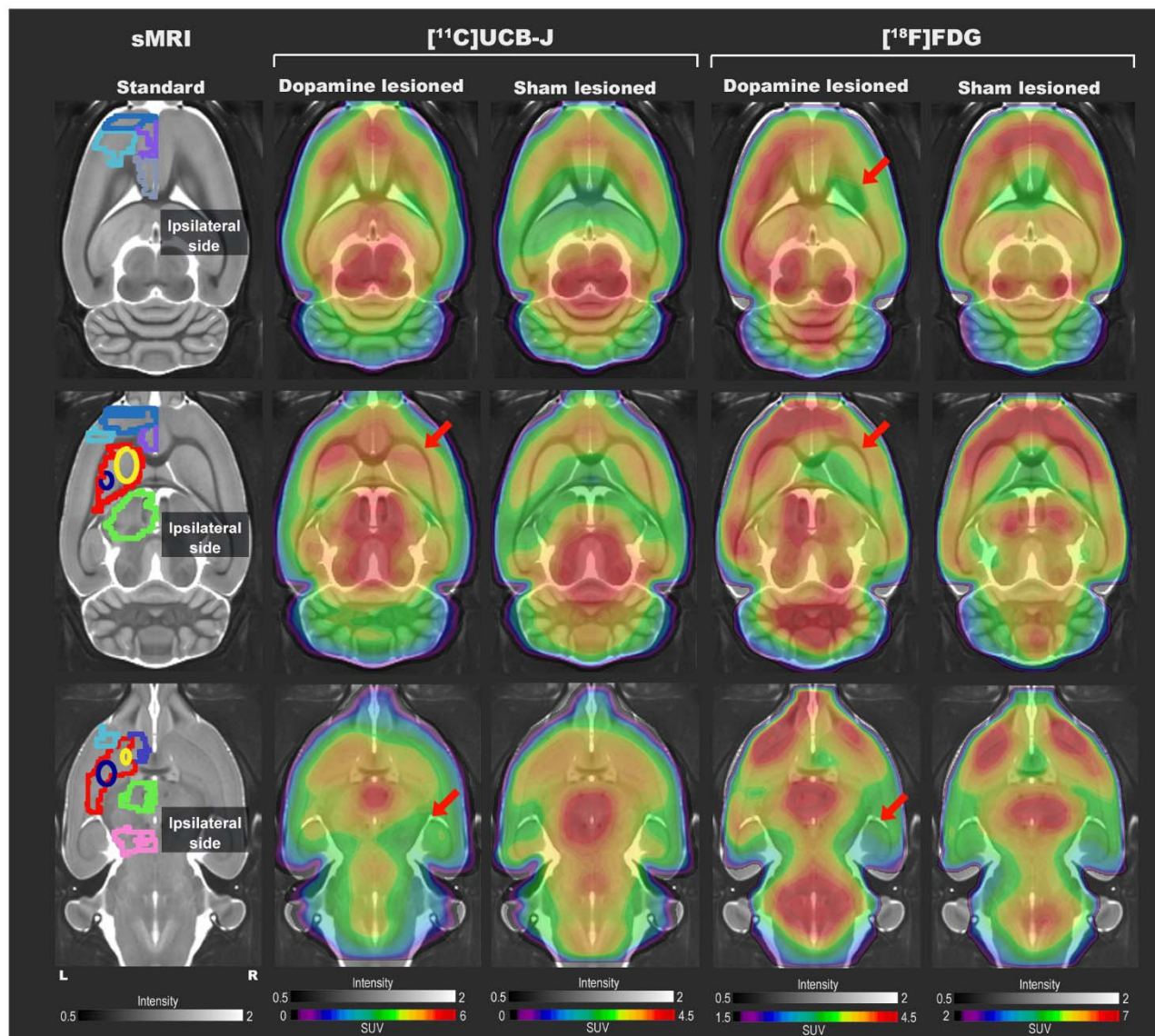


551
552 **Figure 1:** Study design. Eight rats received two intracranial injections of either 6-OHDA or saline in
553 the medial forebrain bundle (MFB) and rostral to substantia nigra and hence divided into two groups
554 sham lesioned (saline) or dopamine lesioned (6-OHDA). Approximately 21 days after the injections,
555 all rats underwent an [¹⁸F]FDG PET scan followed by [¹¹C]UCB-J PET scan 2 days after in a
556 Siemen's high-resolution research tomography (HRRT). All animals were euthanised 30 days after
557 the intracranial injection.



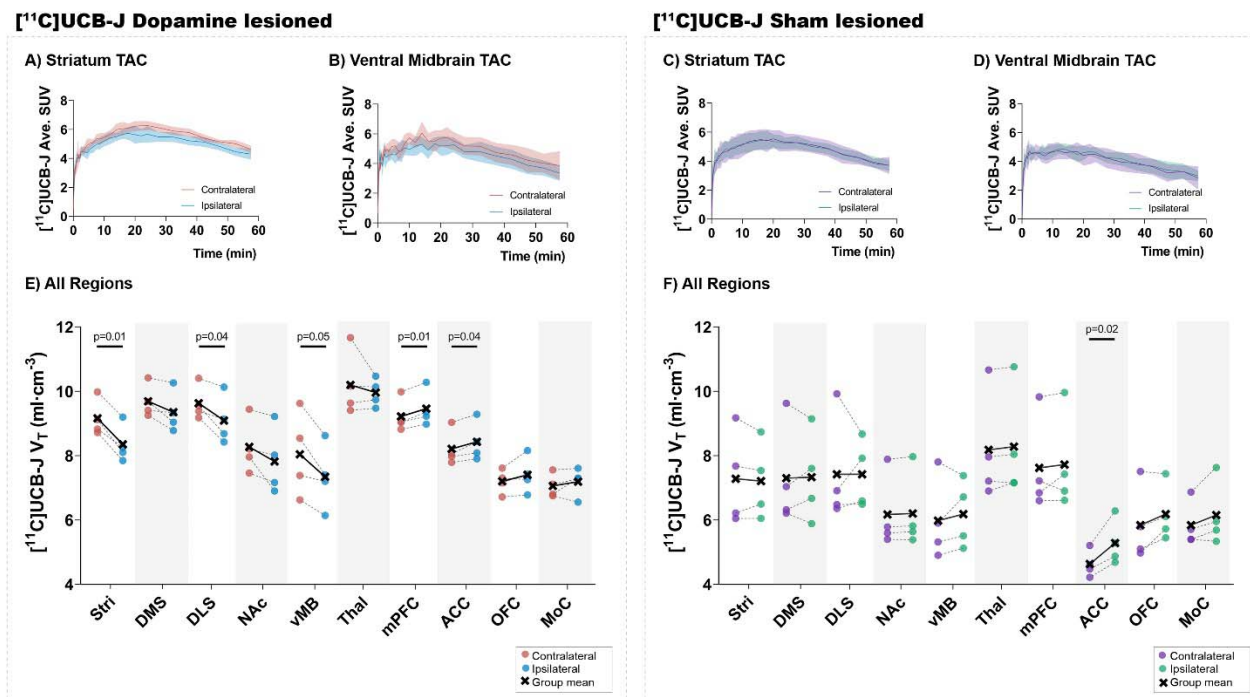
558
559
560
561
562
563
564

Figure 2: Confirmation of 6-OHDA-induced dopaminergic lesions. A) Representative example of tyrosine hydroxylate immunostaining: upper section from sham lesioned rats, lower from dopamine lesioned rats. B) Quantification of the stained area, threshold emphasised in red. C) Quantification of staining intensity, intensity scale insert. D) Quantification of intensity and area relative to contralateral striatum (n = 4/group). Error bar denotes the mean and the 95% confidence interval. P values demonstrated from the Mann-Whitney tests.



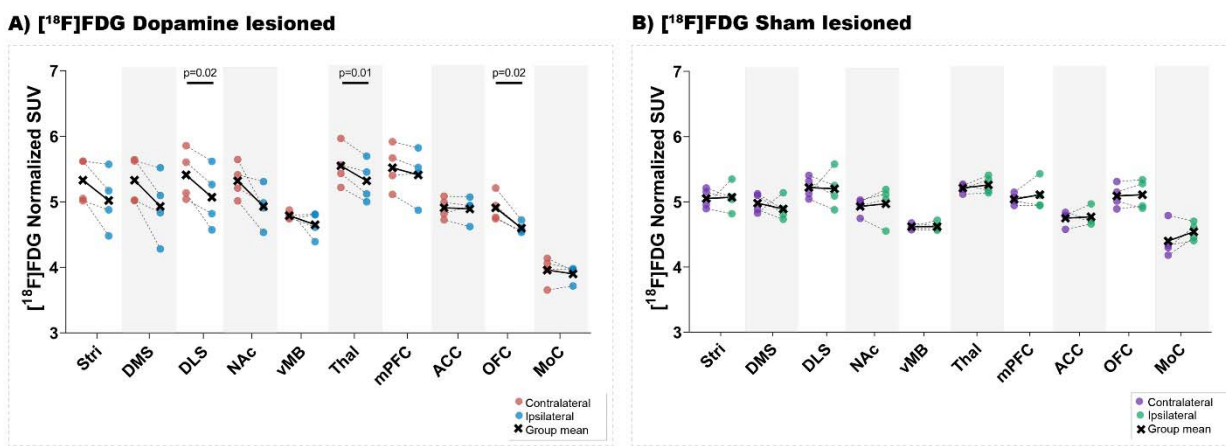
565
566
567
568
569
570
571
572

Figure 3: Representative [¹¹C]UCB-J and [¹⁸F]FDG PET SUV horizontal brain slices from a dopamine and a sham lesioned rat. Standard structural MRI (for illustrative purposes) slices show the selected volumes of interest in one hemisphere; mPFC (medium blue), OFC (purple), motor cortex (light blue), ACC (grey), striatum (red), dorsomedial striatum (yellow), dorsolateral striatum (navy blue), thalamus (green), NAc (dark blue), and ventral midbrain (pink). For [¹¹C]UCB-J, the SUV image represents the sum of 15-60 minutes; for [¹⁸F]FDG, it is the sum of all 45 minutes. The red arrow shows decreased tracer uptake in dopamine lesioned animals.



573
574
575
576
577
578
579
580

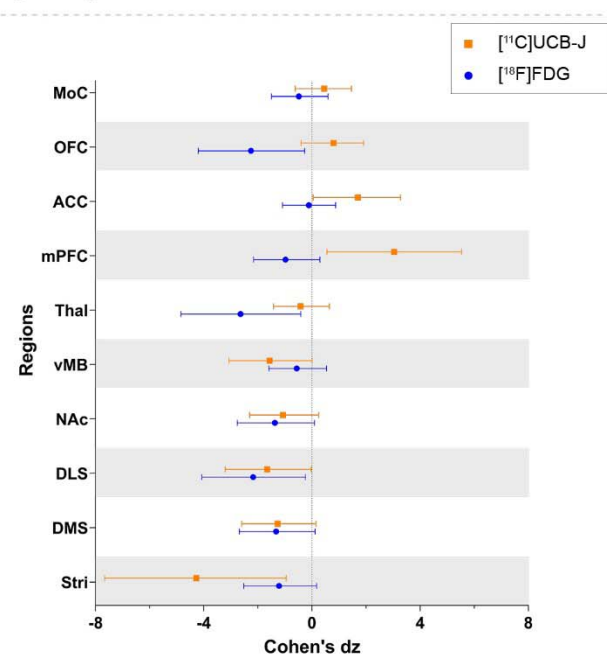
Figure 4: Average [¹¹C]UCB-J binding. Average time-activity curves from all the animals in the striatum (A and C) and ventral midbrain (B and D). Comparison of ipsilateral and contralateral [¹¹C]UCB-J V_T values in the selected regions of interest within the dopamine lesioned (E) and sham lesioned (F) rats. Notable differences are marked with their p values. Stri= striatum, DMS= dorsomedial striatum, DLS= dorsolateral striatum, NAc= nucleus accumbens, vMB= ventral midbrain, Thal= thalamus, mPFC= medial prefrontal cortex, ACC= anterior cingulate cortex, OFC= orbitofrontal cortex, MoC= motor cortex.



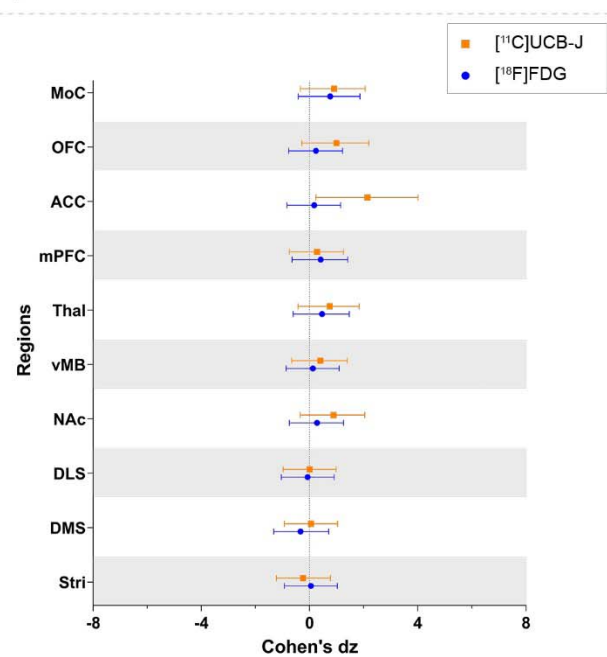
581
582
583
584
585
586
587

Figure 5: [¹⁸F]FDG uptake. Direct comparison between ipsilateral and contralateral hemispheres of normalised [¹⁸F]FDG uptake in all regions of interest within the dopamine lesioned (A) and sham lesioned (B) rats. Notable differences were marked with their uncorrected p values. Stri = striatum, DMS = dorsomedial striatum, DLS = dorsolateral striatum, NAc = nucleus accumbens, vMB = ventral midbrain, Thal = thalamus, mPFC = medial prefrontal cortex, ACC = anterior cingulate cortex, OFC = orbitofrontal cortex, MoC = motor cortex.

A) Dopamine lesioned



B) Sham lesioned



588

589 **Figure 6:** Direct comparison of effect size (Cohen's dz values) as measured by [¹¹C]UCB-J and
590 [¹⁸F]FDG PET. All regions within the dopamine and sham lesioned animals in the study are
591 compared. Error bar denotes the mean and the 95% confidence interval. Stri= striatum, DMS=

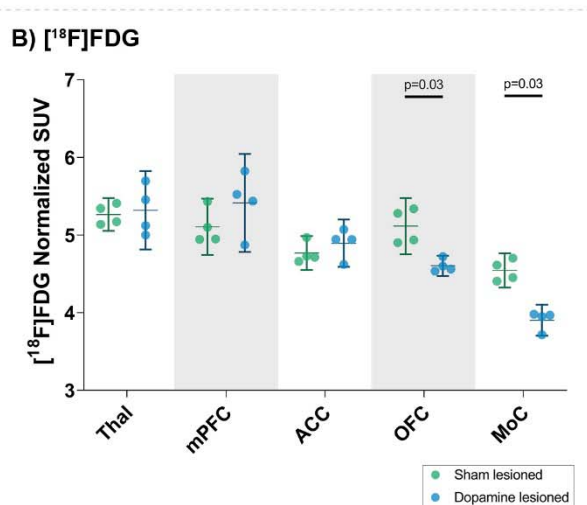
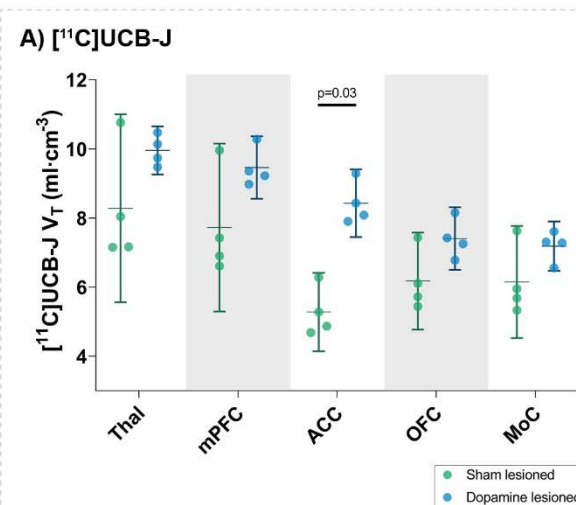
592

593 NAc= nucleus accumbens, vMB= ventral
594 midbrain, Thal= thalamus, mPFC= medial prefrontal cortex, ACC= anterior cingulate cortex, OFC=

595

596

Ipsilateral lesion comparison



597

598 **Figure 7:** Analysis of [¹¹C]UCB-J V_T values (A) and [¹⁸F]FDG (B) uptake in the ipsilateral side of
599 dopamine lesioned and sham lesioned animals. Error bar denotes the mean and the 95% confidence
600 interval. Thal = thalamus, mPFC = medial prefrontal cortex, ACC = anterior cingulate cortex, OFC =
601 orbitofrontal cortex, MoC = motor cortex.